



Research Article

Operating temperature and ruthenium doping influence on the charge carriers type transition in the α -Fe₂O₃ sensors upon liquefied petroleum gases detection

Ntokozo G Cebekhulu^{1*}, Sunday A Ogundipe¹,
Ceboliyazakha L Ndlangamandla¹, Steven S Nkosi² and
Hendrik C Swart³

¹Department of Physics, University of Zululand, Private Bag X1001, KwaDlangezwa ZA3886, South Africa

²Department of Physics, University of Limpopo, Private Bag X1106, Sovenga, ZA0727, South Africa

³Department of Physics, University of the Free State, Box 339, Bloemfontein, ZA9300, South Africa

Received: 28 February, 2024

Accepted: 18 March, 2024

Published: 19 March, 2024

*Corresponding author: Ntokozo G Cebekhulu, Department of Physics, University of Zululand, Private Bag X1001, KwaDlangezwa ZA3886, South Africa, E-mail: ntokozongc200@gmail.com

ORCID: <https://orcid.org/0000-0002-7001-629X>

Keywords: Gas sensing; Charger carrier transition; Dopant concertation; Alpha iron oxide-based sensor; Sensitivity

Copyright License: © 2024 Cebekhulu NG, et al. This is an open-access article distributed under the terms of the Creative Commons Attribution License, which permits unrestricted use, distribution, and reproduction in any medium, provided the original author and source are credited.

<https://www.clinsurggroup.com>



Abstract

Metal oxide-based sensors have been extensively used for environmental monitoring, health, and safety. This work focuses on synthesizing α -Fe₂O₃ and doping it with Ruthenium (Ru) to study its gas-sensing properties over flammable and hazardous gases. An anomalous behavior was observed during the Liquefied Petroleum Gas (LPG). This Ru-doped α -Fe₂O₃ showed a charge carrier switching transition from n- to p-type conductivity due to Ru doping and the sensor's operating temperature. The switching behavior on the Ru-doped samples happened between 3,000 and 4,000 ppm of the LPG concentrations. However, the Ru doping content did not seem to be affecting this transition except to alter the LPG response. The sensors' operating temperature did alter the switching transition from n- to p-type conductivity. The temperatures varied from 175 to 225 °C. Metal Oxide Semiconductor (MOS) based on α -Fe₂O₃ nanoparticle doped with ruthenium (Ru- α -Fe₂O₃) was more selective towards LPG with a gas response of 24.41.

Introduction

The importance of solid-state semiconductor gas sensors in gas analysis and safety applications has attracted substantial attention for more than two decades [1-3] recently, semiconductor nanotechnology has become more prevalent in sensor technology. Metal and semiconductor nanoparticles are basic components of gas-sensitive materials that were used in older and even recent years, and their size-dependents physical properties are very important both in theory and concentration [4-6]. To protect the environment and human health, it is essential to detect and monitor toxic, hazardous

gases [5]. There are many hazardous gases, but liquefied petroleum gas (LPG) is among them [7]. In recent years, gas sensors have gained attention in both research and industry due to the presence of various toxic gases in the air that are harmful to human health [8]. The effects of toxic, hazardous, and flammable gases can include asthma, skin burning, dizziness, cancer, lung issues, and even weight loss [9]. In the atmosphere, every gas has a Threshold Limit Value (TLV), which represents the maximum concentration of respective toxic gases that humans may breathe without harming them, expressed as parts per million (ppm) [10]. It is very important that living creatures, including humans, are safe, so there is a



great demand for gas sensors for detecting toxic and hazardous substances. Among the major causes of global warming and climate change are toxic and flammable gases such as CO, NH₃, LPG, and H₂ [11-14]. These flammable and hazardous gases are important to detect properly using sensors that will be able to comprehend their dynamic behaviors. Globally, household and outdoor pollution caused about 7 million deaths in 2016, making it the 4th leading cause of death [9,15]. According to World Health Organization (WHO) data, air pollution alone caused 4.2 million deaths in 2016, while household air pollution contributed to 3.6 million deaths. Among all environmental risks to human health, air pollution ranks highest in 2019 [13,16]. Because humans spend most of their time indoors, such as in our homes, hospitals, schools, etc., where most flammable and toxic gases including CO₂, CO, Benzene, and toluene are present, indoor air quality is equally important. As a result, air pollution indoors and outdoors must be controlled [16-18]. Humans and other living organisms worldwide must live in a clean and safe environment [19-22]. Any leakage of toxic gases into the atmosphere or environment would pose a health risk to humans [5,23,24]. Gas sensors are classified according to their working principle: infrared IR sensors, metal oxide semiconductor sensors, electrochemical sensors, and optical sensors.

Globally, chemical and gas sensors are attracting increased interest due to the increasing need to monitor gaseous molecules in various applications [25]. A chemo-resistive gas sensor is potentially attractive because of its ease of fabrication, low cost, low detection level (ppm), and simplicity of operation. They are based on measuring the change in electrical resistance and whenever a sensor is exposed to the environment, the electrical resistance changes. In recent years, Metal Oxide Semiconductors (MOS) such as TiO₂, SnO₂, WO₃, and Fe₂O₃ have attracted great attention due to their wide range of applications [19,24,26,27]. A good gas sensor is classified by the following parameters that determine the quality of a gas sensor: sensitivity, selectivity, operating temperature, and reproducibility. Alpha iron oxide (α -Fe₂O₃) has been used as a catalyst, pigment, and gas sensor because of its low cost, corrosion resistance, and environment-friendly properties. It is one of the most stable phases with n-type semiconducting properties (e.g. 2.1 eV) [11,26,28,29]. α -Fe₂O₃ has a rhombohedral crystallizer structure, with lattice parameters of a = 0.5035 nm and C = 1.37489 nm [30], And it has been utilized as a material for sensing a variety of gases, including CO, ethanol, acetone, hydrogen, formaldehyde, acetic acids, and ammonia [29,31]. α -Fe₂O₃ particles have been synthesized using a variety of techniques, including the sol-gel approach [32,33], Hydrothermal techniques [34-37], chemical vapor depositions [34], and Co-precipitation methods [11,34]. In those synthesis methods, factors including reactant concentration, reaction time, temperature relations, and the material's iron salt control the size and shape of the products. Additionally, the advantages of chemical precipitation procedures include quick preparation times, high purity, high homogeneity, low costs, well-crystallized products, and relatively low reaction rates [34,38]. However, in this work, we report on the synthesis of α -Fe₂O₃ and Ru- α -Fe₂O₃ with a different percentage of Ru to

validate the transition of n-type to p-type of the material at different operating temperatures of the material. The sensors were fabricated by drop casting method in the laboratory. In this work we are reporting on the switching transition of the chemo-resistive sensors surface majority charge carriers from n-to-p types or vice versa of α -Fe₂O₃ and Ru- α -Fe₂O₃.

To date, most n-type/p-type switching transitions can only happen for both oxidizing and reducing environments of the various sensors through the temperature variations of the gas concentration variation in the presence of humidity [23,31]. The n-type to p-type is only observed when the is temperature variation and gas concentration variation. Specifically, the switching of n-type to p-types of α -Fe₂O₃ pure and Ru- α -Fe₂O₃ occurs at the different concentrations at a fixed temperature of 225 °C. While the LPG concentration varied from 1000 to 2000 ppm n-type is observed material, and the transition normal started at 3000 ppm, and the p-type was observed from 4000 to 1000 ppm of the LPG concentration. Similar ways were used for the Ru- α -Fe₂O₃ with 0.05 wt% at the fixed operating temperature of 225 °C to observe the switching transition material. The addition of Ru also affects the occurrence of the transition in the material. For the Ru- α -Fe₂O₃ sample with 0.05 wt%, an n-type transition occurs when the LPG concentration varies from 1000 to 3000 ppm, and the transition normally starts from 4000 ppm of LPG concentration while the p-type was observed while the LPG concentration was varied from 5000 to 10000 ppm. Further, an increase in the percentage of Ru to 0.10 wt% affects the position of the switching of the transition of the material from n-type to p-type. It was observed that while the LPG concentration varies from 1000 to 2000 ppm it shows n-type, the switching of the transition occurs at 3000 ppm and the p-type was observed while the concentration varies from 5000 to 10000 ppm of LPG. This simply means that the switching of n-type to p-types depends on the operating temperature and the concentration of the target gas.

In this work, the target gas was found to be LPG since it shows a higher response compared to other gases being used in the work. The operating temperature of pristine α -Fe₂O₃ and Ru- α -Fe₂O₃ was decreased to 200 °C to further study the charge carrier switching from n-type to p-type. While the LPG concentration varied from 1000 to 6000 ppm n-types were observed, and the transition started to occur at a high concentration of LPG starting from 7000 ppm, the p-type transition was observed when LPG concentrations varied from 8000 to 10000 ppm. Reducing the operating temperature further to 175 °C causes the delay in switching transition from n- to p-type. The switching transition takes place when the operating temperature of the sensor is reduced.

Experimental procedure

Synthesis: Chemical precipitation has been identified as the desired route to prepare the samples of α -Fe₂O₃ and Ru-Fe₂O₃ with different percentages. Iron (III) chloride hex hydrate (FeCl₃.6H₂O) is the precursor while the ammonia solution (NH₂OH) is the precipitating agent. The sample was washed with ethanol, and all the solutions were prepared with distilled water. In a beaker, 100 ml of deoxygenated distilled water was mixed with



Iron (III) Chloride hex hydrate ($\text{FeCl}_3 \cdot 6\text{H}_2\text{O}$). The magnetic stirrer was used to stir the solution for 30 minutes while the temperature was fixed to 80 °C to obtain 0.01 M which is the concentration of the solution. To determine the effect of concentration on the size of the material, a similar method was used to obtain (0.1 M) for the other solutions of Ru- $\alpha\text{-Fe}_2\text{O}_3$. Ammonia hydroxide (NH_4OH) was used as a precipitating agent, added drop by drop gradually until pH 11 was reached. Under constant magnetic stirring, the solution was heated for 3 hours. The precipitated product was collected by centrifugation (6000 rpm) machine. The product was washed several times with ethanol and distilled water. After that, the product was dried for 3 hours at 80 °C in an oven. The product was calcined in the open air for 4 hours at 700 °C to convert FeOOH to obtain $\alpha\text{-Fe}_2\text{O}_3$.

Characterization of hematite and Ru dope hematite: The crystal structure of those powders was characterized by X-ray diffraction (XRD), by using a German Bruker D8 instrument with Cu/K as a radiation source with wavelength ($\lambda = 1.5418 \text{ \AA}$), and data were collected in the range of 10 °C to 80 °C at a scanning speed of 0.5, which equivalent to 45 minutes per samples. An image of the surface morphology and particle size of the powder was captured by scanning electron microscopy (SEM, ZEISS Sigma VP-03-07). The high-resolution transition electron microscopy (HR-TEM) of the samples was done using the JEOL 1400 instrument. The thermal behavior was evaluated by Thermo gravimetric (TGA) and differential thermal analysis (DTA) in the air by using TGA Q500 TA systems or instruments. The chemical state of the samples was examined by using A PHI5400 Versaprobe X-ray Photoelectron Spectroscopy (XPS) with monochromatic Al K α (1486.7eV) X-ray at a pressure less than 10⁻⁸ mbar. The surface area and pore size were determined by a nitrogen adsorption /desorption isotherms analyzer. Nitrogen adsorption/desorption Isotherms of the adsorbent samples were carried out on a 77 k Micrometrics TRISTAR II 3020 volumetric adsorption analyzer.

Sensor fabrication and measurement: To investigate the gas sensing properties of $\alpha\text{-Fe}_2\text{O}_3$ and Ru- $\alpha\text{-Fe}_2\text{O}_3$, the powder samples were sonicated for 2 hr in the ultra-sonicate bath, after the drop-casting method was used to drop the samples on alumina substrate screen-printed with a gold electrode on the top. The sensor was allowed to dry to remove the organic residual at the temperature of 120 °C. The gas sensing measurement was conducted by using a KS026K16 (KENOSISTES model of the 2016 year). Sensors were placed inside the gas testing chamber equipped with electrical and gas feeds for sensing measurement. The measurement was conducted at various operating temperatures (225 °C, 200 °C, and 175 °C). The voltage on the system was set to 5.0 V throughout the measurements. Inside the chamber, the concentration of the target gases was controlled by the flow of the dry air (79% N₂ and 21% O₂). LPG, NH₃, ethanol, propanol, and hydrogen sulfide (H₂S) were the target gases. Dry air was used as a carrier gas to dilute the target gases. Dry air was first introduced into the chamber for 30 minutes for the sensor to attain an equilibrium state, and then after that, each concentration of a target gas was introduced into the chamber for 10 minutes. Then dry air was

introduced in the chamber again for 10 minutes for the sensor to recover. This was done for all gas-sensing measurements. The Keithley 6487/E pico ammeter /Voltage source was used to quantify the current of the sensor, and the electrical response (S) of the sensor was calculated by the following equation: where I_g and I_a represented the current in the target gas and the current in the air respectively as shown in the equation.

$$S = \frac{I_g}{I_a} - 1 \quad (1)$$

Where I_g and I_a represented the current in the target gas and the current in the air respectively.

Results and discussion

X-ray diffraction and surface morphology

Figure 1a shows the XRD pattern of $\alpha\text{-Fe}_2\text{O}_3$ and Ru- $\alpha\text{-Fe}_2\text{O}_3$ samples. Only nine peaks were observed on the XRD pattern, however, only five peaks have high intensity; these include the peaks located at (012), (104), (110), (116), and (300). Two of the peaks, i.e., the one situated at (113) and (204) show lower intensity. It implies the formation of the hematite having a rhombohedral structure with the lattice parameter $a = 0.5036 \text{ nm}$, and $c = 1.3749 \text{ nm}$. In ruthenium-doped samples (Ru- $\alpha\text{-Fe}_2\text{O}_3$), the peak located at the plane (104) began to decrease in intensity upon the addition of ruthenium until 0.15 wt% Ru and increased thereafter. Similarly, the peak is located at the plane (110). As the percentage of Ru increased the secondary phase (RuO₂) was formed and observed at $2\theta = 28.267$. The formation of the secondary phase (RuO₂) at an early Ru loading can be attributed to the fact that Ru has much bigger atomic radii (2.8222 Å) than that of Fe with 2.0885 Å. The average crystallite size of pristine $\alpha\text{-Fe}_2\text{O}_3$ and Ruthenium doped $\alpha\text{-Fe}_2\text{O}_3$ was calculated by using the Debye-Scherrer equation. Pristine $\alpha\text{-Fe}_2\text{O}_3$ has a bigger crystallite size than Ru- $\alpha\text{-Fe}_2\text{O}_3$ Samples (Figure 1b). Alpha iron oxide (Hematite) exhibits a wide variety of properties including excellent chemical stability surface activity and semiconductor properties. It is the most stable iron oxide with a bandgap of (E.g. 2.2 eV) It is also widely used as a gas sensing material for toxic and harmful gases since it is a promising material in gas sensing. Under ambient conduction, hematite is easy to synthesize due to its magnetic properties such as corrosion resistance, low cost, and low toxicity.

The crystallite size calculated using Scherrer's equation in Figure 1b shows a decrease with the Ru loading onto the $\alpha\text{-Fe}_2\text{O}_3$ matrices until 0.10 Ru. Thereafter it begins to increase.

Figure 1c-1e shows the surface morphology obtained by using the SEM of $\alpha\text{-Fe}_2\text{O}_3$ and Ru- $\alpha\text{-Fe}_2\text{O}_3$. The surface morphology on (c) is for the pure $\alpha\text{-Fe}_2\text{O}_3$. While (d-e) is the surface morphology of Ru- $\alpha\text{-Fe}_2\text{O}_3$. With Ru = 0.05 wt % and Ru = 0.20 wt %. The image of the surface morphology indicates the formation of the material with small spherical particles (Figure 1c-1e). It can be seen in Figure 1c-1e that increasing the Ru concentration creates pores on the $\alpha\text{-Fe}_2\text{O}_3$ surfaces and less agglomeration.

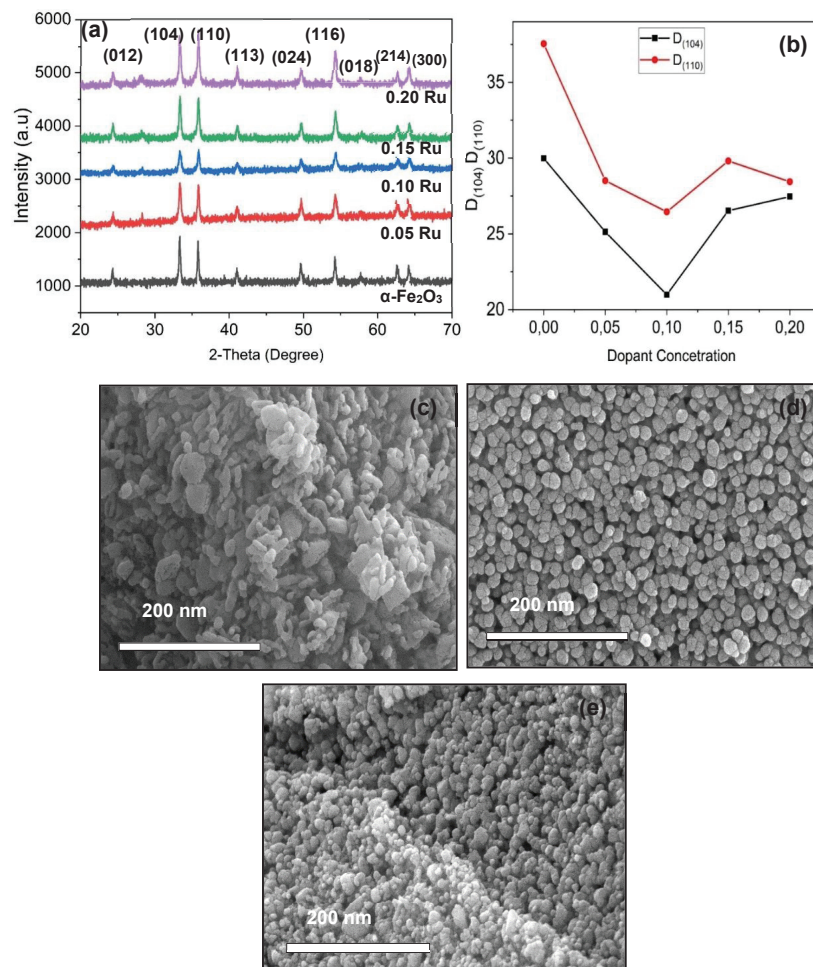


Figure 1: (a) The XRD patterns of pristine ($\alpha\text{-Fe}_2\text{O}_3$) and (Ru- $\alpha\text{-Fe}_2\text{O}_3$) samples (b) Crystallite sizes estimated from the (104) and (110) dominant peaks. SEM images of $\alpha\text{-Fe}_2\text{O}_3$ pure and Ru- Fe_2O_3 samples with (c) Ru = 0.05 wt. %, (d) Ru = 0.10 wt. %, and (e) Ru = 0.20 wt. %.

The insets of Figure 2 show the selected area electron diffractions (SEAD) patterns corresponding to the HRTEM images of $\alpha\text{-Fe}_2\text{O}_3$ and Ru- $\alpha\text{-Fe}_2\text{O}_3$ samples. The interplanar distance or d-spacing was calculated from the diffraction ring of the samples and the values of 0.256 nm were found on the most prominent rings indexed (110) crystalline plane of $\alpha\text{-Fe}_2\text{O}_3$ nanoparticles. The bright rings in the SAED patterns (Figure 2) confirm the crystallinity of alpha iron oxide ($\alpha\text{-Fe}_2\text{O}_3$) samples. This is consistent with the data analysis of XRD (Figure 1a). To confirm the growth pattern of the crystallites and also to verify the distribution of the crystallites, the average particle size of the as-prepared powder was measured using the HR-TEM. Figure 2 shows the results of that experiment. Since the majority of the nuclei in the nanoparticles are attached to large Meso- Fe_2O_3 crystals, HR-TEM images were used to confirm their identification.

To determine whether sample surfaces are meso- or macroporous, nitrogen adsorption-desorption measurements were conducted. Figure 3 shows nitrogen adsorption-desorption isotherm curves of the pristine $\alpha\text{-Fe}_2\text{O}_3$ and Ru- Fe_2O_3 . Nitrogen adsorption-desorption isotherms measure the specific surface area and pore size of sample samples. Isotherm curves have been observed for the samples in the range 0.85 to 1.0 p/

po. with H4 hysteresis loops. Inset Figure 3. Shows the pore size distribution of the material calculated from desorption isotherms by using the Barrecc- Joyner-Halenda model (BJH). And, it shows that the material mainly contains a 50-nm meso-pore [39].

X-ray photoelectron measurements were carried out better to understand the material's surface and chemical makeup. The PHI 5000 Scanning (ESCA) microprobe system was used.

The sample of $\alpha\text{-Fe}_2\text{O}_3$ and Ru- $\alpha\text{-Fe}_2\text{O}_3$ were measured for XPS and underwent survey scans. In particular, the survey demonstrates the elements found in the materials depicted in (Figures 4,5). But most importantly it confirmed the presence of Fe, O, and Ru in the materials. The narrow scan was done on both samples, pure and doped. Figure 4 XPS result for $\alpha\text{-Fe}_2\text{O}_3$. The survey scan shows three elements present in the sample of $\alpha\text{-Fe}_2\text{O}_3$, namely, O1s, Fe2p, and Ru3d as shown in Figure 4a, Then each element was further investigated by XPS to confirm the binding energy of each presented in Figure 4b-4d. The Fe2p scan in Figure 4b shows only three peaks that correspond to the following binding energy, respectively 710.1 eV, 711.5 eV, and 725.1 eV. The high peaks occur when the binding energy is lower, at 710.1 eV. The scan for O1s and Ru3d is shown in Figure

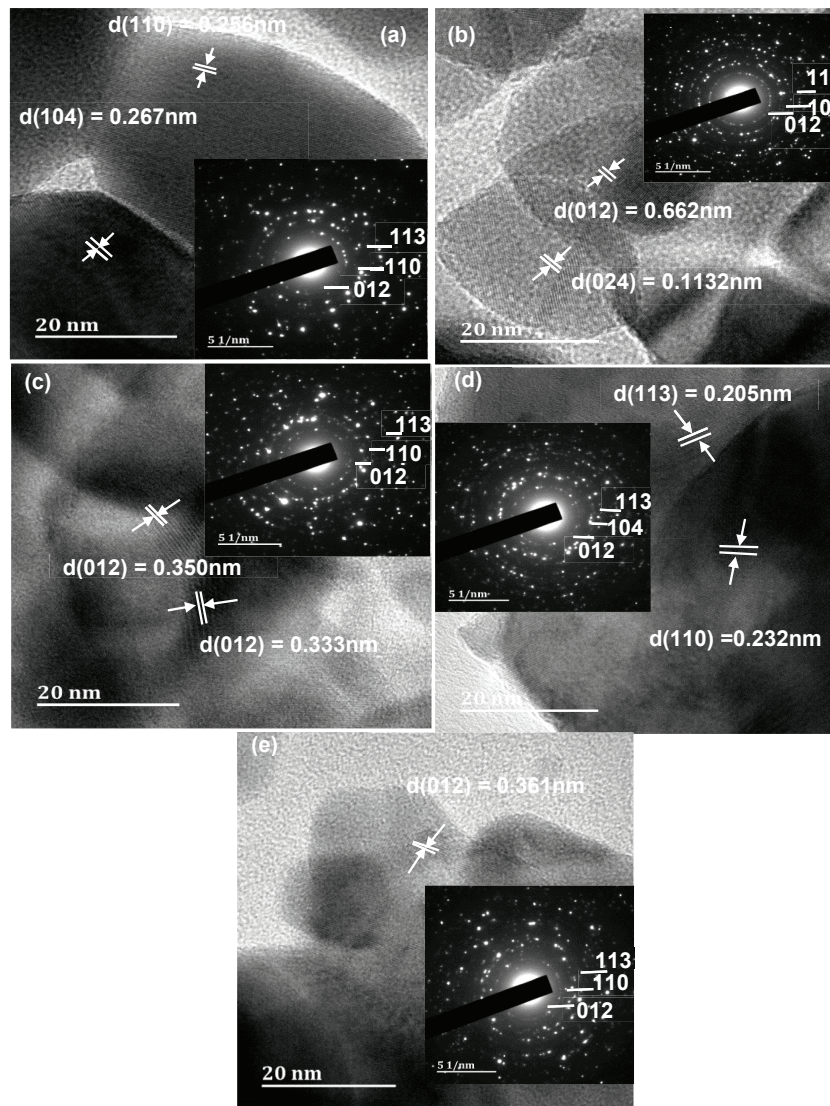


Figure 2: HRTEM images of α -Fe₂O₃ and Ru-Fe₂O₃ nanostructure (a) Ru = 0.0 wt %, (b) Ru = 0.05 wt %, (c) Ru = 0.10 wt %, (d) Ru = 0.15 wt % and (e) Ru = 0.20 wt %. The insets are the corresponding selected area electron diffraction patterns.

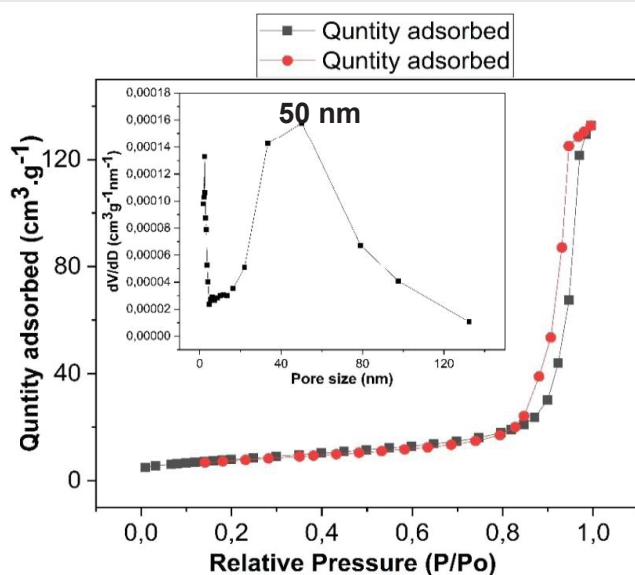


Figure 3: N₂ adsorption-desorption isotherm of the pristine alpha iron oxide nanoparticles. The inset corresponds to the pore size distribution.

4c-4d shows only two peaks, but for the O1s high peaks occur at the lower binding energy of 530.0 eV. The lower energy peak 530.5 eV is the lattice oxygen (O_l) while the high energy peak 532.5 eV is chemisorbed oxygen species (O_c). For the Ru3d the high peak occurs when the binding energy is high, at 285.1 eV.

Figure 5 Represent the result of XPS for Ru- α -Fe₂O₃ (0.05 wt %). The survey scan for all samples doped with Ru is given in Figure 5a. Ru- α -Fe₂O₃ (0.05 wt %) shows only three scans, which are Fe2p, O1s, and Ru3d. This is presented in Figure 5b-5d. The scan Fe2p of Ru- α -Fe₂O₃ shows only three peaks, corresponding to binding energy 712.1 eV, 715.0 eV, and 725.1 eV. The high peaks occur at the lower binding energy of 712.1 eV, this is presented in Figure 5b. Comparing this with the Fe2p for α -Fe₂O₃ shows that by increasing the concentration of Ru the position of the peaks and broadening of the peaks is affected. The O1s scan shows only two peaks, which correspond to binding energy 529.4 eV and 532.5 eV (Figure 5c). The lower energy peak 529.4 eV is the lattice oxygen (O_l) while the high energy peak 532.5 eV is chemisorbed oxygen species (O_c).

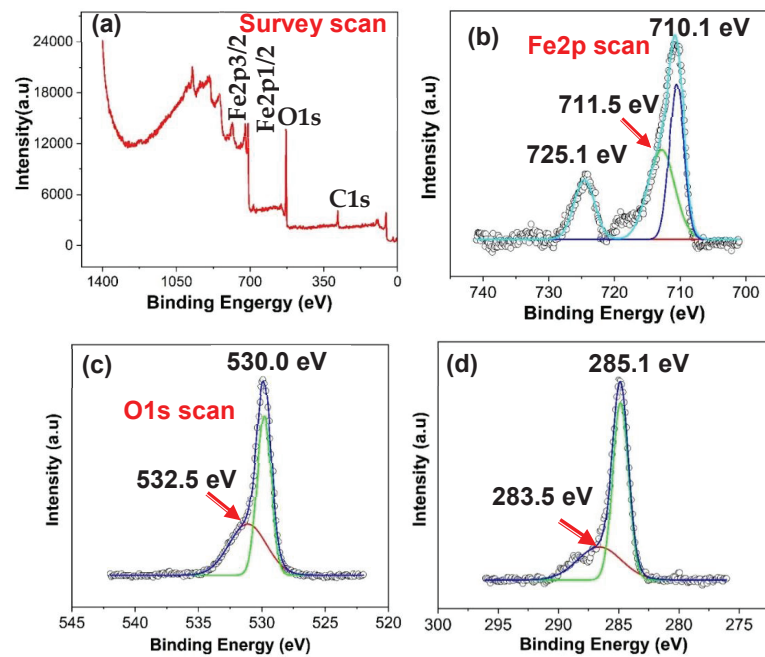


Figure 4: XPS results for $\alpha\text{-Fe}_2\text{O}_3$ sample, (a) Survey scan, (b) Fe2p scan, (c) O1s scan, and (d) Ru 3d scan.

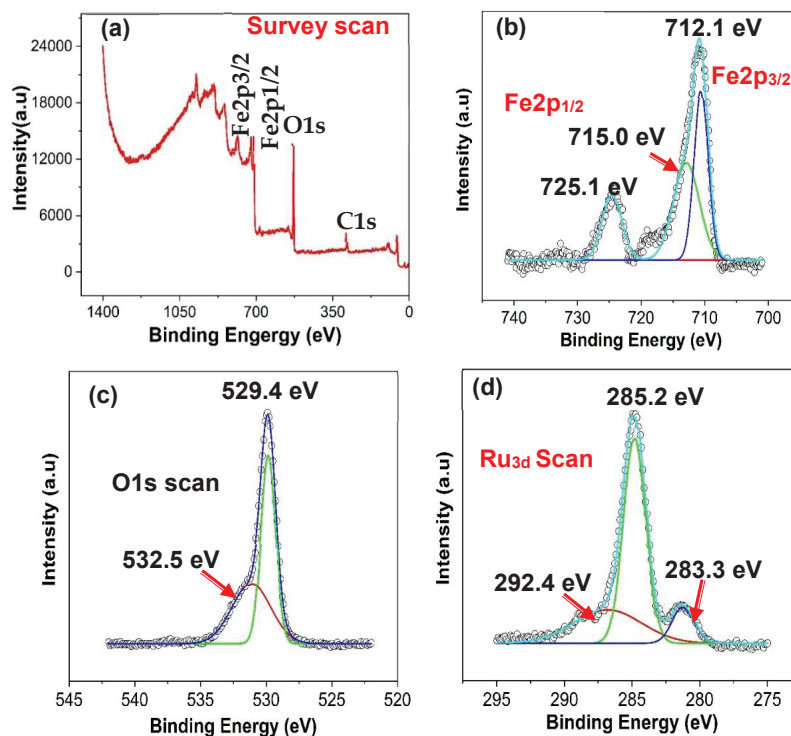


Figure 5: XPS results of $\alpha\text{-Fe}_2\text{O}_3\text{-Ru}$ (0.05 wt %) samples (a) Survey scan, (b) Fe2p scan, (c) O1s scan, and (d) Ru 3d scan.

The Ru3d scan for Ru- $\alpha\text{-Fe}_2\text{O}_3$ shows only three peaks, corresponding to the following binding energy: 292.4 eV, 285.2 eV, and 283.3 eV. By comparing it to $\alpha\text{-Fe}_2\text{O}_3$ Ru3d it shows that if the binding energy is 285.2 eV there is a development of the new peak with due addition of Ru this is represented in Figure 5d.

Gas sensing part

Figure 6a shows the gas-sensing characteristics of semiconducting metal oxides when exposed to flammable and toxic gases at an optimum operating temperature. The selectivity plot of the different flammable gases is shown in (Figure 6b). The 3D plot in (Figure 6b) shows the sensors'

response (S) of pristine $\alpha\text{-Fe}_2\text{O}_3$ and Ru- Fe_2O_3 samples. Ammonia (1000 ppm) was substantially detected by the pristine $\alpha\text{-Fe}_2\text{O}_3$ - based sensor, with a response of 24.410 at 225 °C operating temperature. However, the sensor's response towards ammonia (NH_3) decreases upon the addition of ruthenium, and the selectivity shifts towards Liquefied Petroleum Gas (LPG).

The influence of the operating temperature and gas concentration on the occurrence of charge carrier transition was observed. $\alpha\text{-Fe}_2\text{O}_3$ is an n-type semiconductor based on the existing study. In this work, we are reporting on the

switching of n-type -to-p- type that occurs at different operating temperatures. Figure 7 shows the sensor response patterns of the $\alpha\text{-Fe}_2\text{O}_3$ and Ru- Fe_2O_3 samples at the fixed operating temperature of 225 °C. By further reducing the operation temperature to 200 °C and 175 °C it caused the delay in the transition of the n-p type's material. In Figure 7b from 1000 ppm and 5000 pm n-types semiconductor was observed and the switching of the material starting from 6000 ppm to 7000 ppm and from 8000 ppm to 10000 ppm p-types was observed. While the operating temperature was 175 °C in Figure 7c from 1000 ppm to 9000 ppm only n-types were observed and the transition of switching started at a later stage with the

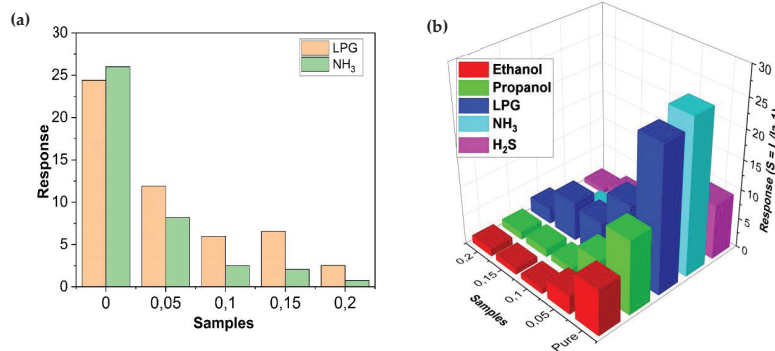


Figure 6: (a) Sensors' response towards LPG and NH_3 at the operating temperature of 225 °C, and (b) Selectivity 3D plot of n-type $\alpha\text{-Fe}_2\text{O}_3$ and Ru- Fe_2O_3 toward various flammable gases (ethanol, propanol, ammonia, hydrogen sulfide, and liquefied petroleum gas (LPG)) at 225 °C operating temperature.

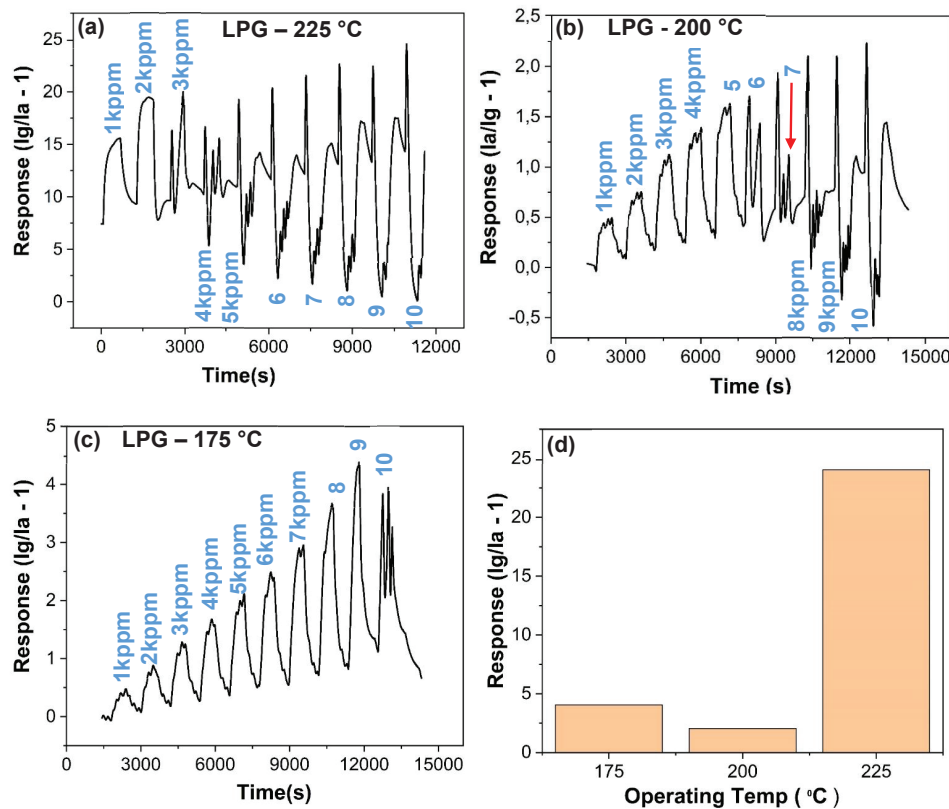


Figure 7: Response pattern of the pristine $\alpha\text{-Fe}_2\text{O}_3$ at an operating temperature of (a) 225 °C, (b) 200 °C, and (c) 175 °C. (d) Response/operating temperature relation plot of the pristine $\alpha\text{-Fe}_2\text{O}_3$.

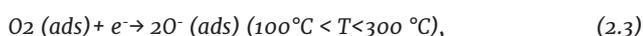


concentration of LPG was 10 000 ppm this due to decreasing in the operating temperature. In Figure 7a, α -Fe₂O₃ oxide shows n-type behavior while the concentration of the LPG varied from 1000 to 3000 ppm, the transition or switching started when the concentration was 4000 ppm and α -Fe₂O₃ exhibited p-type characteristic from LPG concentrations of 5000 to 10 000 ppm. Further increase in Ru percentage affected the position of the transitions and it caused the delay in the Transition of the material from n-p types also the gas sensing response was decreased upon the addition of the ruthenium in the alpha iron oxide (Figure7b-7c). Figure7b shows that while the operating temperature was set up at 225 °C the gas sensing response was much better compared to 200 °C and 175 °C. This simply means that the sensor was stable at high temperatures as all materials have the unique operating temperature.

Sensing mechanism of alpha iron oxide doped with ruthenium

Normally, gas sensing takes place only at the surface of the semiconducting material that contains the oxygen being chemically adsorbed by the reaction. However, the chemisorbed oxygen on the surface of α -Fe₂O₃ is normally ionized by capturing the free electron from the conduction band, which increases the resistance in the air by creating the depletion layers [40]. The atmospheric oxygen captures the free electrons on the sensor material to become O₂⁻, O⁻, or O⁻² depending on the operating temperature [23].

Whenever n-type semiconductors like hematite and graphite are exposed to a target gas, the previously created electron-depletion layers when the sensor is in the air become thin, and electrons return to the conduction band. In the beginning, the oxygen molecules from the air pass through the surface of the hematite and are adsorbed to the surface. Following this, the oxygen-free electrons form oxygen ions on the hematite surface with trapped electrons, as indicated in the following chemical reactions [19,23,41,42].



In this work, the optimal operating temperature was 225 °C, hence the dominant chemisorbed oxygen species were O_(ads)⁻ (See Eq. 2.3). During the chemical gas Sensing measurements, α -Fe₂O₃ oxide-based sense was exposed to LPG (a reducing gas) at an operating temperature of 225 °C. Since this sensor is an n-type, the LPG reacts with the adsorbed oxygen O_(ads)⁻ to transfer electrons back to the alpha-iron Conduction band. The material exhibited p-type characteristics under various LPG concentrations, and this caused some delay in the formation of the n-to-p-type transition of the material. (Eq. 2.5–2.7) explain how the LPG interacts with the oxygen inside the chamber. When the LPG is introduced into the chamber, the reducing gas reacts with the adsorbed oxygen species (anions),

a series of complex reactions take place, and ultimately LPG gets oxidized.

These reactions (Eqs. 2.5–2.7) cause a significant amount of free electrons to be released, increasing the sensor current.



Conclusion

The α -Fe₂O₃ and Ru- α -Fe₂O₃ based sensors were fabricated, with various percentages of Ruthenium, in this study. Testing was done on different flammable gases, including LPG, propane, ammonia, ethanol, and hydrogen sulfide (H₂S) for both α -Fe₂O₃ and Ru- α -Fe₂O₃ samples. In this experiment, α -Fe₂O₃ exhibited a switching n-p transition at the operating temperature of 225 °C upon LPG detection. The results of the experiment showed that ammonia exhibited high sensitivity and selectivity. However, upon the addition of Ru in alpha iron oxide, the selectivity, and sensitivity shifted to Liquefied petroleum gas (LPG) (Figure7a). The operating temperature of the system was controlled to study the occurring anomalous n-p switching transition. By further decreasing the operating temperature of the system to 200 °C and 175 °C it was observed that the n-p switching transition depends on the operating temperature. As shown (in Figure7b-7c)) n-p switching transition was delayed at a lower operating temperature of 200 °C and only five cycles showed n-types material while the switching transition of starting between the concentration of 6000 to 7000 ppm of LPG, and it was further observed that only three cycles show p-types material from 8000 to 1000 ppm. This suggests that a further decrease in operating temperature will lead to further delay in the occurrence of the n-p type carrier transition, though the sensor's response might reduce, and is shown in Figure 7c. In addition, increasing the concentration of the LPG caused a delay in the formation of the transition of the material this is shown in Figure7b.

Finally, it was discovered that ruthenium is unsuitable for use as a dopant material because it reduces the gas-sensing response. It was discovered that the pure alpha iron oxide phase reacted with ammonia more favorably. The selectivity changed in Favor of Liquefied Petroleum Gas (LPG) as ruthenium concentration increased. This is due to the fact the atomic radii of Ru have the biggest atomic radii of 2.8222 while the Fe shows the smallest atomic radii. This results in the decrease of the gas response of the material while the concentration of the ruthenium increases. Each material has a unique operation temperature, hence in the study, the better result was observed when the operating temperature of the system was high at 225 °C. At the lower temperatures of 200 °C and 175 °C it was observed that the gas sensing response was also decreasing with the temperature this is presented in Figure 7d.



Acknowledgment

The authors wish to thank the research office at the University of Zululand for the financial support during the cause of this work. The National Research Foundation is also duly acknowledged for its consistent support to carry out research nationwide. Finally, the authors wish to acknowledge the University of the Free State for helping us with XPS measurements of the material.

References

- Mirzaei A, Leonardi S, Neri G. Detection of hazardous volatile organic compounds (VOCs) by metal oxide nanostructures-based gas sensors: A review. *Ceramics International*. 2016; 42(14): 15119-15141.
- Korotcenkov G. Metal oxides for solid-state gas sensors: What determines our choice? *Materials Science and Engineering: B*. 2007; 139(1):1-23.
- Neri G. First fifty years of chemoresistive gas sensors. *Chemosensors*. 2015; 3(1):1-20.
- Mizsei J. Gas Sensors and Semiconductor Nanotechnology. *Nanomaterials (Basel)*. 2022 Apr 12;12(8):1322. doi: 10.3390/nano12081322. PMID: 35458029; PMCID: PMC9032215.
- Franke ME, Koplin TJ, Simon U. Metal and metal oxide nanoparticles in chemiresistors: does the nanoscale matter? *Small*. 2006 Jan;2(1):36-50. doi: 10.1002/sml.200500261. Erratum in: *Small*. 2006 Mar;2(3):301. PMID: 17193551.
- Mirzaei A. Metal-core@ metal oxide-shell nanomaterials for gas-sensing applications: a review. *Journal of Nanoparticle Research*. 2015; 17:1-36.
- Nkosi S. The effect of stabilized ZnO nanostructures green luminescence towards LPG sensing capabilities. *Materials Chemistry and Physics*. 2020; 242:122452.
- Akram R, Saleem M, Farooq Z, Yaseen M, Almohaimeed ZM, Zafar Q. Integrated Capacitive- and Resistive-Type Bimodal Relative Humidity Sensor Based on 5,10,15,20-Tetraphenylporphyrinatonicel(II) (TPPNI) and Zinc Oxide (ZnO) Nanocomposite. *ACS Omega*. 2022 Aug 21;7(34):30590-30600. doi: 10.1021/acsomega.2c04313. PMID: 36061702; PMCID: PMC9434763.
- Dhall S. A review on environmental gas sensors: Materials and technologies. *Sensors International*. 2021; 2:100116.
- Akram R, Saleem M, Farooq Z, Yaseen M, Almohaimeed ZM, Zafar Q. Integrated Capacitive- and Resistive-Type Bimodal Relative Humidity Sensor Based on 5,10,15,20-Tetraphenylporphyrinatonicel(II) (TPPNI) and Zinc Oxide (ZnO) Nanocomposite. *ACS Omega*. 2022 Aug 21;7(34):30590-30600. doi: 10.1021/acsomega.2c04313. PMID: 36061702; PMCID: PMC9434763.
- Cuong ND. Gas sensor based on nanoporous hematite nanoparticles: effect of synthesis pathways on morphology and gas sensing properties. *Current Applied Physics*. 2012; 12(5):1355-1360.
- Jeong SY, Jang D, Lee MC. Property-based quantitative risk assessment of hydrogen, ammonia, methane, and propane considering explosion, combustion, toxicity, and environmental impacts. *Journal of Energy Storage*. 2022; 54:105344.
- Sovacol BK. Climate change and industrial F-gases: A critical and systematic review of developments, sociotechnical systems and policy options for reducing synthetic greenhouse gas emissions. *Renewable and sustainable energy reviews*. 2021; 141:110759.
- Hosseini SE, Wahid MA. Development of biogas combustion in combined heat and power generation. *Renewable and Sustainable Energy Reviews*; 2014; 40:868-875.
- Tran VV, Park D, Lee YC. Indoor Air Pollution, Related Human Diseases, and Recent Trends in the Control and Improvement of Indoor Air Quality. *Int J Environ Res Public Health*. 2020 Apr 23;17(8):2927. doi: 10.3390/ijerph17082927. PMID: 32340311; PMCID: PMC7215772.
- Organization WH. Ten threats to global health in 2019. 2019; 2019.
- Chmielewski A. Monitoring, Control, and Effects of Air Pollution. *BoD- Books on Demand*. 2011.
- Abbasi YF, Bera H. Konjac glucomannan-based nanomaterials in drug delivery and biomedical applications, in *Biopolymer-Based Nanomaterials in Drug Delivery and Biomedical Applications*. Elsevier. 2021;119-141.
- Mkwae PS. The heat rate kinetics on the liquefied hydrocarbon gases sensing and food quality control detecting strategy. *Materials Chemistry and Physics*. 2022; 277:125550.
- Vermesan O, Friess P. Internet of things: converging technologies for smart environments and integrated ecosystems. *River Publishers*. 2013.
- Raworth K. A safe and just space for humanity: can we live within the doughnut? *Oxfam*. 2012.
- Percival RV. Environmental regulation: Law, science, and policy [connected EBook with study center]. *Aspen Publishing*. 2021.
- Nkosi SS. Abnormal p-type to n-type switching during nitric oxide gas sensing: Ni (OH) 2 nanoplatelets on amorphous NiO seed layers. *Vacuum*. 2022; 200: 111032.
- Gallo F, Fossi C, Weber R, Santillo D, Sousa J, Ingram I, Nadal A, Romano D. Marine litter plastics and microplastics and their toxic chemicals components: the need for urgent preventive measures. *Environ Sci Eur*. 2018;30(1):13. doi: 10.1186/s12302-018-0139-z. Epub 2018 Apr 18. PMID: 29721401; PMCID: PMC5918521.
- Tingting Y. Highly sensitive H₂S detection sensors at low temperature based on hierarchically structured NiO porous nanowall arrays. *Journal of Materials Chemistry A*. 2015; 3(22):11991-11999-2015 v.3 no.22.
- Hien VX. High acetone-sensing performance of bi-phase α - γ -Fe₂O₃ submicron flowers grown using an iron plate. *Journal of Science: Advanced Materials and Devices*. 2021; 6(1): 27-32.
- Cruz-Yusta M, Sánchez M, Sánchez L. Metal Oxide Nanomaterials for Nitrogen Oxides Removal in Urban Environments. *Tailored Functional Oxide Nanomaterials: From Design to Multi-Purpose Applications*. 2022; 229-276.
- Jing Z, Wang Y, Wu S. Preparation and gas sensing properties of pure and doped γ -Fe₂O₃ by an anhydrous solvent method. *Sensors and Actuators B: Chemical*. 2006; 113(1):177-181.
- Zhang F. Controlled synthesis and gas-sensing properties of hollow sea urchin-like α -Fe₂O₃ nanostructures and α -Fe₂O₃ nanocubes. *Sensors and Actuators B: Chemical*. 2009; 141(2):381-389.
- Tadic M. Magnetic properties of mesoporous hematite/alumina nanocomposite and evaluation for biomedical applications. *Ceramics International*. 2022; 48(7):10004-10014.
- Govardhan K, Grace AN. Metal/metal oxide doped semiconductor based metal oxide gas sensors—A review. *Sensor letters*. 2016; 14(8): 741-750.
- Lan F. Preparation and characterization of SnO₂ catalysts for CO and CH₄ oxidation. *Reaction Kinetics, Mechanisms and Catalysis*. 2012; 106(1): 113-125.
- Hassan HS. Fabrication and characterization of gas sensor micro- arrays. *Sensing and Bio-Sensing Research....* 2014; 1:34-40.
- Lassoued A. Synthesis, structural, morphological, optical and magnetic characterization of iron oxide (α -Fe₂O₃) nanoparticles by precipitation



method: effect of varying the nature of precursor. *Physica E: Low-dimensional Systems and Nanostructures*. 2018; 97:328-334.

35. Jazirehpour M, Khani O, Jafari M. Hydrothermal synthesis of Al-doped magnetite nanoflakes and the effect of aspect ratio on their magnetic properties. *Physica B: Condensed Matter*. 2022; 414238.
36. Landolsi Z. Synthesis and characterization of porous TiO₂ film decorated with bilayer hematite thin film for effective photocatalytic activity. *Inorganic Chemistry Communications*. 2022; 109865.
37. Hung CM. Synthesis and gas-sensing characteristics of α -Fe₂O₃ hollow balls. *Journal of Science: Advanced Materials and Devices*. 2016; 1(1):45-50.
38. Lassoued A. Control of the shape and size of iron oxide (α -Fe₂O₃) nanoparticles synthesized through the chemical precipitation method. *Results in physics*. 2017; 7:3007-3015.
39. Murugesan B. Fabrication of palladium nanoparticles anchored polypyrrole functionalized reduced graphene oxide nanocomposite for antibiofilm associated orthopedic tissue engineering. *Applied Surface Science*. 2020; 510:145403.
40. Wang C, Yin L, Zhang L, Xiang D, Gao R. Metal oxide gas sensors: sensitivity and influencing factors. *Sensors (Basel)*. 2010;10(3):2088-106. doi: 10.3390/s100302088. Epub 2010 Mar 15. PMID: 22294916; PMCID: PMC3264469.
41. Shoji NN. Extremely sensitive and selective flammable liquefied hydrocarbon gas sensing and inter-dependence of fluctuating operating temperature and resistance: Perspective of rare-earth doped cobalt nanoferrites. *Journal of Alloys and Compounds*. 2021; 859:157846.
42. Li C, Liang Y, Mao J, Ling L, Cui Z, Yang X, Zhu S, Li Z. Enhancement of gas-sensing abilities in p-type ZnWO₄ by local modification of Pt nanoparticles. *Anal Chim Acta*. 2016 Jul 13;927:107-16. doi: 10.1016/j.aca.2016.04.050. Epub 2016 Apr 28. PMID: 27237843.

Discover a bigger Impact and Visibility of your article publication with Peertechz Publications

Highlights

- ❖ Signatory publisher of ORCID
- ❖ Signatory Publisher of DORA (San Francisco Declaration on Research Assessment)
- ❖ Articles archived in worlds' renowned service providers such as Portico, CNKI, AGRIS, TDNet, Base (Bielefeld University Library), CrossRef, Scilit, J-Gate etc.
- ❖ Journals indexed in ICMJE, SHERPA/ROMEO, Google Scholar etc.
- ❖ OAI-PMH (Open Archives Initiative Protocol for Metadata Harvesting)
- ❖ Dedicated Editorial Board for every journal
- ❖ Accurate and rapid peer-review process
- ❖ Increased citations of published articles through promotions
- ❖ Reduced timeline for article publication

Submit your articles and experience a new surge in publication services

<https://www.peertechzpublications.org/submission>

Peertechz journals wishes everlasting success in your every endeavours.